A direct fragmentation method with Weibull function distribution of sizes based on finite- and discrete element simulations

Adriana Paluszny[a,*], XuHai Tang[b], Morteza Nejati[a], Robert W. Zimmerman[a]

[a]*Department of Earth Science and Engineering, Imperial College, London, United Kingdom*
[b]*Department of Civil and Environmental Engineering, Princeton University, Princeton, NJ, United States of America*

Abstract

A direct method is proposed to rapidly fragment bodies during impulse-based discrete element method simulations of multiple body interactions. The approach makes use of patterns and size distributions obtained both from experiments, and from numerical models that rigorously compute fragmentation by growing fractures explicitly. Weibull parameters approximate the fragment size distributions as a function of body size and relative contact velocity. Structured domain decomposition is applied on the colliding bodies directly, resulting in a low-cost fragmentation calculation that depends on relative velocity, but which does not require the computation of fracture growth nor explicit element de-bonding, but instead classifies pre-existing mesh elements into the newly fragmented sub-domains. The method is applied to the fragmentation of a single spherical rock fragment, to an irregularly shaped rock fragment, and to the crushing of an array of spherical rock fragments.

Keywords: discrete element method, fragmentation, Weibull distribution, fracture pattern, finite element, impulse

1. Introduction

Fragmentation occurs in a variety of situations, ranging from the breakage of a single micro galena grain, of size 1- 2.5 mm (Ali and Bradshaw, 2011), as part of comminution in mineral processing, up to huge geological faults in the Earth's brittle crust, with fragmentation occurring in the kilometer scale (Holland et al., 2006). Fragmentation of solids is a fundamental mechanics problem in industries involving processing, transportation and storage of particulate materials, mining and blasting, comminution techniques including grinding, milling and crushing (Djordjevic and Morrison, 2006; Tromans, 2008), rapid excavation and underground structures, rockfall mitigation techniques (Wang, 2009), and exploration drilling for oil, gas and mineral reservoirs.

Brittle fragmentation, in which cracks initiate and propagate at locations of stress concentration, has been addressed experimentally using dynamic, impact, and static loading for a variety of specimen shapes (Chau et al., 2000; Salman et al., 2002; Wu et al., 2004). Experimental procedures to investigate impact-induced fragmentation typically utilize spherical particles, due to their simple shape and low cost experimental setup. The two main impact loading experiments

*Corresponding author. Tel.: +44 20 7594 7435, fax: +44 20 7594 7444.
Email address: apaluszn@imperial.ac.uk (Adriana Paluszny)

reported in the literature are the drop-shatter and the double impact tests (Table 1). The drop-shatter test consists in impacting spherical solids on a target with different velocities (Cheong et al., 2003; Salman et al., 2004), whereas the double-impact test is the dynamic counterpart of the static diametral compression of spheres between two rigid platens (Chau et al., 2000; Wu et al., 2004). Experiments using non-spherical solids include the fragmentation of cubes (Giacomini et al., 2009), cylinders (Shockey et al., 1974), slabs (Grange et al., 2008), and beams (Riou et al., 1998). Physical experiments are restricted to specific scales, materials, geometries, and impact velocities.

Numerical methods provide means to investigate fragmentation quantitatively, under conditions that are difficult to reproduce in the laboratory. The most widely used approach is the discrete element method (DEM) (Cundall and Strack, 1979), followed by mesh free (Belytschko et al., 1994) and finite element (FEM) methods (Paluszny and Zimmerman, 2013), and combinations thereof, such as FEM/DEM (Munjiza et al., 1995). Mesh-free methods have been applied to simulate fragmentation in the context of aeronautics research, including plugging failures at high-speed impacts (Ren and Li, 2010), ductile fracture in large scale shell structures (Ren and Li, 2012), and on-orbit spacecraft breakup dynamics simulation (Zhang et al., 2013). Further applications of the mesh-free method to fragmentation include the simulation of high velocity concrete fragmentation (Rabczuk and Eibl, 2003), modelling of hypervelocity impact of steel (Libersky et al., 1997), and fragmentation of granular media by impulse loads (Lai et al., 2015). The material point method (Sulsky et al., 1994), which uses Lagrangian solid particles embedded in an Eulerian grid, has been applied to address fragmentation of exploding cylinders (Banerjee, 2004).

In DEM, fracturing is modeled as the de-bonding of adjacent elements due to compressive stress waves (Wang and Tonon, 2010, 2011; Wittel, 2010). The impact of circular disks in 2D against frictionless plates is the most common specification to investigate dynamic fragmentation using DEM (Khanal et al., 2004; Kun and Herrmann, 1998; Potapov and Campbell, 1994, 1997, 2001; Salman and Gorham, 2000; Thornton et al., 1996) (see Table 2). 3D DEM fragmentation simulations have been reported for agglomerate particles (Kafui and Thornton, 2000; Thornton et al., 1999), sphere impact (Bruchmüller et al., 2011; Carmona et al., 2008; Potapov and Campbell, 2001; Wittel, 2010), and dynamic compression (Wang and Tonon, 2010). The combination of the discrete and finite element methods (FEM/DEM) (Munjiza et al., 1999, 2011) captures deformation of individual DEM bodies, and de-bonding decomposition of DEM bodies. 2D FEM/DEM has been applied to model sphere fragmentation (Camacho and Ortiz, 1996), to block caving advance and caving-induced surface subsidence (Vyazmensky et al., 2007), rock slope analysis (Xiang et al., 2009), and in the context of blast fragmentation due to gas expansion (Munjiza et al., 2000). The main disadvantage of DEM is that it is penalty based, and, thus, requires time-consuming and error-prone calibration of micro- to macro- properties which must be performed for each material individually. Fractures cannot be explicitly defined, and materials often artificially behave as particulates or agglomerates. Thus, mechanical rock properties such as the Young's modulus and Poisson's ratio cannot be directly used to predict deformation. Moreover, 3D fragmentation simulations and qualitative pattern evaluation are scarce in relation to the maturity of DEM, possibly due to the lack of realism caused by the absence of a fracture mechanics-based crack growth model.

Methods that apply enrichment functions in the context of fracture propagation simulation (Sukumar et al., 2000),

include the extended finite element method (XFEM) (Belytschko and Black, 1999) and cracking particle method (Rabczuk and Belytschko, 2004). XFEM has been successfully developed to model arbitrary branched and intersecting cracks (Daux et al., 2000) and three-dimensional multi-scale crack propagation (Holl et al., 2014). The cracking particle method adds enrichment functions into the global approximation of conventional FEM to consider the crack tips and crack boundaries. However, fractures are represented implicitly by a set of point-based enriched functions (Rabczuk et al., 2007, 2004). Even though the former are widely used to model fracturing, they are rarely applied to model fragmentation.

FEM-based growth has been used in combination with the impulse-based DEM to investigate fragmentation in three dimensions (Paluszny et al., 2013). As opposed to classic DEM methods, impulse methods base collisions directly on geometry and impact trajectory, as well as on material properties such as toughness, Young's modulus, and Poisson's ratio (Tang et al., 2014). Therefore, this approach avoids handling mesh interpenetration, avoids applying arbitrary penalties, and avoids the costly definition and calibration of micro-elastic properties. Furthermore, in contrast to DEM fragmentation models, which model fracture growth as a loss of cohesion between elements, the FEM-based discrete fracture approach models propagation as a function of stress intensity factor concentrations around crack tips (Paluszny and Zimmerman, 2011). Although accurate, this method requires the computation of the displacement field due to compressive forces that result during fragment interaction, and computes stress intensity factors at the tips of existing fractures to predict growth. During the simulations, growth results in geometric evolution of the fracture surface, which in turn requires re-meshing of the domain (Paluszny and Zimmerman, 2013). Computing stress fields within each fragment at each step of the dynamic simulation precludes large simulations involving hundreds and thousands of bodies. Simplifications of this method have been published in the context of block caving to estimate the effect of fragmentation on predictions of draw point hang-up (Tang et al., 2013b).

A direct method for the numerical simulation of fragmentation is presented in the present paper, which draws from the advantages of both DEM and FEM simulations. Specifically, it seeks to resolve collisions accurately, and apply fragmentation patterns based on estimated impact velocities. The approach draws from existing physical and numerical experiments, and does not require re-meshing, as do explicit fracturing propagation simulations. Instead, colliding bodies are fragmented based on the application of fragmentation patterns directly, and domain decomposition is applied in real time. The size distribution and size of the largest ensuing bodies due to fragmentation are controlled by the impact velocity-dependent Weibull parameters (Cheong et al., 2004; Lu et al., 2002b; Shih, 1980; Wittel et al., 2008), and satisfy, by construction, the Weibull distribution that is widely accepted to describe the fragmentation behavior of brittle materials.

2. Fragmentation Patterns

Fragmentation can be defined as the process of reduction of a solid size by breaking it into smaller parts. According to fractographic observations on rock fragments, the mechanism of fragmentation involves the following four stages

(Shockey et al., 1974): (1) Activation of pre-existing flaws, (2) Propagation of activated cracks, (3) Crack coalescence and branching, and (4) Isolation of fragments leading to fragmentation.

As a result of fragmentation, a number of new domains, fragments, are produced. Estimating their size and shape is of interest in engineering applications. A characteristic fragmentation pattern, originally defined for rock blasting (Kutter and Fairhurst, 1971) can also be defined by (a) a comminuted or crushing zone around the contact, (b) a damaged zone with dense micro-cracking around the crushing zone, and (c) a further zone where dominant cracks develop.

Similar patterns can be found in the fragmentation of brittle solids due to impact loading. As a result of the impact of spherical solids, a crushed zone is developed just below the contact area, surrounded by a region where several macro-cracks usually break the solid (Chau et al., 2000; Salman et al., 2004; Santurbano and Fairhurst, 1991). When the impact force is high, the material is significantly deformed by the high compressive and shear stresses under the contact area. Many small cracks are generated, and the material tends to break into minute fragments due to crushing. Possible crushing mechanisms include comminution due to high shear stress below the contact area, crack initiation and propagation at the interface between densified and non-densified material, and crack initiation due to high compressive surface stresses at inhomogeneities of the surface (Doyoyo, 2002; Gorham and Salman, 2005). The boundary of the crushed region is roughly conical, defined by shear stress trajectories under high compressive stress at the contact area. Finite element simulations have confirmed that stresses within a roughly hemispherical region under the contact area are much higher than any yield or fracture properties of the material (Gorham and Salman, 2005).

Similar mechanisms of failure have been observed in impact experiments of spheres made of glass (Gorham and Salman, 2005; Salman and Gorham, 2000), concrete (Schubert et al., 2005; Tomas et al., 1999), rock (Santurbano and Fairhurst, 1991), aluminum oxide (Salman et al., 2004), and plaster (Chau et al., 2000). A “cone and slice” fracture pattern has been reported in impact experiments of limestone spheres (Santurbano and Fairhurst, 1991) (Fig. 1). The name refers to two cones of finely broken and crushed material under the contact area, and intact material at the free end of the sphere. Orange-like slices form at the remaining part of the sphere, orthogonally to the impact. The general pattern of fragmentation in concrete samples is also similar to that of glass and rock spheres (Schubert et al., 2005; Tomas et al., 1999).

Numerical studies validate their fragmentation simulations using either fragment mass distributions or qualitative analyses of fragmentation patterns. In both impact and explosion, 2D fragment mass distributions have been found to follow a power law distribution that is independent of impact angle for low impact velocities, whereas high impact velocities yield an exponential fragment size distribution (Behera et al., 2005; Kuna and Herrmann, 1996). Thus far, DEM has not been able to reproduce the dependency of fragment size distribution on the strain rate, although such dependency is clearly observed in experimental results (Wang and Tonon, 2011).

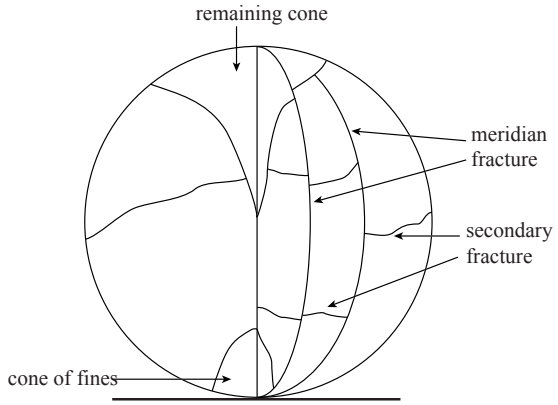


Figure 1: Fragmentation pattern (adapted from Tomas et al. (1999)).

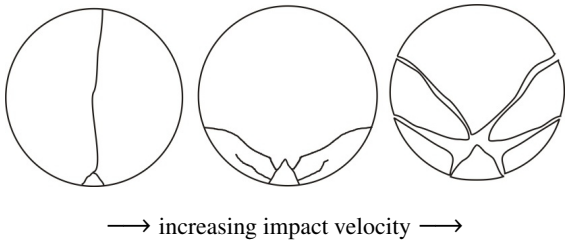


Figure 2: Fragmentation modalities at increasing impact velocities (adapted from Salman et al. (2004)).

2.1. Fragment size distribution

Fragment size distribution is commonly used to evaluate fragmentation in solids based on the statistical distribution of fragment size and the fragment size average. For the fragmentation of fine-producing brittle materials, fragment distributions are represented by plots of the cumulative mass in a range of size against fragment size, often reported as quasi-linear graphs for a log cumulative mass against log size (Grady, 2010).

Physical experiments (Arbiter et al., 1969; Gilvarry and Bergstorm, 1961; Oddershede et al., 1993; Turcotte, 1986), stochastic analyses (Åström, 2006; Åström et al., 2000; Åstrom et al., 2004), and forward simulations (Inaoka and Takayasu, 1996; Kun and Herrmann, 1998; Linna et al., 2005) all suggest that for small fragments, size distributions follow a power law function. The exponent of the power law function has also been found to be universal with respect to the material, and independent of the way that energy is imparted to the system, but has been found to depend on the dimensionality of the object (Turcotte, 1986; Wittel, 2010). Deviation from the power-law distribution for large fragment masses has also been modelled by using an exponential cut-off, and employing a bi-linear or Weibull distribution (Antonyuk et al., 2006; Carmona et al., 2008; Cheong et al., 2004; Lu et al., 2002a; Meibom and Balslev, 1996; Oddershede et al., 1993; Potapov and Campbell, 1997). The two-parameter Weibull equation has been widely used to characterize fragment size distribution. Cheong et al. (2004) fitted experimental data to the two-parameter Weibull

equation, for various velocity and impact angles. In all cases, the coefficients of determination were calculated to be greater than 0.98 (Cheong et al., 2003). Fundamental parameters contributing to post-fragmentation size distributions are impact velocity, impact angle, shape, scale, and material.

2.2. Impact velocity and angle

Failure modes are classified into low, intermediate and high velocity regimes (Salman et al., 2004) (Fig. 2). Experiments on spherical samples have shown that failure under impact occurs above a specific threshold velocity, v_l, which depends on the material properties, and decreases with increasing specimen size (Andrews and Kim, 1999; Gorham and Salman, 2005; Salman et al., 2002). The critical normal impact velocity, v_l, is the minimum required velocity to observe physical damage or failure. It is estimated with a static compression test, and is a function of material properties and failure loads (Cheong et al., 2003; Maxim et al., 2006). A second threshold velocity, v_u, can be identified above which solids disintegrate into fine powder (Gorham and Salman, 2005; Salman et al., 2002). When the solid velocity is between v_l and v_u, different failure modes occur, leading to systematic variation in their fragmentation size distribution.

Fragmentation patterns obtained from low velocity impact are similar to those observed in static compression and indentation tests, indicating that failure occurs within the framework of the quasi-static stress regime, since the impact duration is long compared to the propagation time of stress waves throughout the sphere (Gorham and Salman, 2005). As sphere size increases, v_l drops, indicating that decreasing the particle diameter increases the velocity needed to break them (Salman et al., 2002). Unlike low and intermediate velocities, for which the form of failure depends significantly on size and material, high velocity impact usually results in a unique type of fragmentation, irrespective of the form of lower velocities. A wide range of experimental results on the spheres made of soda-lime glass and polymethyl methacrylate (PMMA) demonstrated that despite yielding various failure modes for low velocity impact, spheres exhibit a consistent form of fragmentation for high velocity impact (Gorham and Salman, 2005). Glass, PMMA, aluminium oxide, solid granules, polystyrene, nylon, hard wood, sapphire, tungsten carbide, aluminium, copper and steel, were all found to fail in a similar form at high velocity impact (Salman et al., 2004).

Along with velocity, impact angle also influences the fragmentation pattern. Experiments on spherical samples have shown that under normal impact cracks propagate and divide the sphere symmetrically, while oblique impact results in the formation of unsymmetrical fracture about the impact axis (Cheong et al., 2003). In oblique impact, the normal component of impact velocity is responsible for rupture, while the tangential one only affects the symmetry condition of fragmentation (Gorham and Salman, 2005; Maxim et al., 2006; Salman et al., 2004).

2.3. Shape, scale and material

Physical and material properties of solids influence the force history at the impact moment as well as the failure mechanisms at fragmentation (Wang and Tonon, 2011; Wu et al., 2004). The impact of two rigid bodies results in a very small impact duration and very large impact load. Conversely, the impact duration, and impact force, would be

very large and small, respectively, when two impacting bodies deform with low stiffness. Salman et al. (2002) showed that target material property and thickness can have a very marked effect on particle fragmentation, suggesting that the stiffer target results in more damage in particles. The following characteristics of materials can affect the failure mechanisms in impacted specimens (Gorham and Salman, 2005; Salman et al., 2002): (a) Sensitivity to strain rate; (b) Sensitivity to hydrostatic pressure; (c) Heterogeneity and anisotropy of the material.

According to the theoretical stress analysis and experimental observations on impacted spheres, crack initiation occurs adjacent to the contact area (Schönert, 2004), and crack propagation depends on the original stress field, especially the principal stress trajectories. The fragmentation of impacted spheres exhibit different patterns in elastic and inelastic material behavior (Schönert, 2004). During the elastic behavior of the material, a significant tensile stress is developed on the contact area periphery directed perpendicular to it, leading to initiation of cleavage cracks, *i.e.* ring cracks and divergent cone cracks. These cracks propagate along the principal stress trajectories, bending outward in directions to the surface. This process generates fine fragments underneath the contact area, and a large cone shaped fragment at the opposite side of contact area (Fig. 2). The formation of fines is due to the high stress energy density in the region underneath the contact area. The large cone-shaped fragment is also developed due to tending cracks to bend outward and propagate in the direction to the surface. Pushing the cone of fine to the sphere also leads to generating and propagation cleavage cracks in meridional planes, resulting in production of the orange-slice shape fragments (Fig. 1). Experimental observations in glass (Cheong et al., 2003; Salman and Gorham, 2000), limestone (Santurbano and Fairhurst, 1991) and concrete (Arbiter et al., 1969; Khanal et al., 2008; Tomas et al., 1999) have confirmed this pattern for fragmentation of spheres.

Shape and scale of the specimens have also been found to influence the fragmentation patterns. As mentioned earlier, the larger the sphere, the lower the threshold velocity v_l. The experimental results on fragmentation patterns have been mainly reported for spherical specimens. Nevertheless, the limited investigations on non-spherical samples have suggested a complete different fragmentation pattern from the spherical ones (Giacomini et al., 2009).

3. Methodology

A method is now presented to directly model fragmentation as a result of collision. The method applies collision patterns to impacting bodies based on impact velocity, shape, scale, and material. Collisions among multiple bodies are resolved using an energy consistent impulse-based discrete element method (Tang et al., 2013a, 2014). Contact detection (Lin and Canny, 1991) is based on the computation of the relative normal velocities of colliding bodies at each contact point. The change of relative velocity is computed from collision resolution, which is used to generate the fragmentation pattern. Weibull parameters are interpolated from experimental and physical data, which are a function of the maximum change of compressive relative velocity.

3.1. Impulse-based discrete element method dynamics

The dynamics simulation is based on Newton's laws of motion and the energy tracking method (ETM) (Tang et al., 2014); a generalized form of the impulse based method which ensures energy conservation (Tang et al., 2013a) during multiple object, multiple contact resolution (see Fig. 3). The impulse discrete element method does not require nor allow objects to penetrate during the dynamics simulation. Instead, contact time is predicted based on speed and trajectory (Lin and Canny, 1991; Mirtich and Canny, 1995), and impulses are applied to avoid penetration and model collision. ETM provides an efficient and accurate alternative to resolve high-frequency collisions among hundreds and thousands of colliding bodies, without making use of arbitrary penalty parameters, while ensuring that collisions are modelled in an energy consistent manner. The latter is of particular interest in the simulation of block caving systems, as the energy of the collision is distributed between ore dynamics and fracture-driven fragmentation (Paluszny et al., 2013; Tang et al., 2013b).

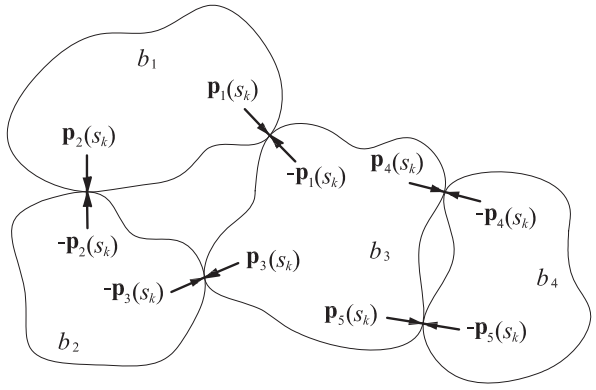


Figure 3: Collision of multiple bodies: multiple bodies, $\mathbf{b} = \{b_0, b_1, ..., b_m\}$, collide with multiple contact points $\mathbf{c} = \{c_0, c_1, ..., c_n\}$, m is the total number of colliding bodies and n is the total number of contact points. A set of impulses, $(\mathbf{p}_0(s_k), \mathbf{p}_1(s_k), ...\mathbf{p}_n(s_k))$, are applied to contact points at iteration s_k.

Fig. 3 illustrates the problem posed by the multiple collision, $\mathbf{c} = \{c_0, c_1, ..., c_n\}$, interaction between multiple bodies, $\mathbf{b} = \{b_0, b_1, ..., b_m\}$, detected at a time step t_c, where m is the number of colliding bodies and n is the number of contact points. When resolving these collisions using ETM, multiple collisions are treated as concurrent collisions at each iteration, and impulses are computed and applied to contact points sequentially. The interaction of multiple collisions is simulated by iterating until all relative normal velocities are non-negative.

3.2. Geometry and discretization

Fragments are represented volumetrically. Each body is discretized by a set of tetrahedral elements in an arbitrary and unstructured manner. Seeding-based pattern fragmentation does not increase the number of elements during the simulation, as the original discretization is maintained. Therefore, the size of the smallest fragments is capped by the size of the smallest element of the original mesh.

3.3. Local coordinate system

Under compression, normal splitting is the primary mode of failure, as observed in the crushing of granular materials (Lee and Farhoomand, 1997; Mesri and Vardhanabhutib, 2009), the fragmentation of falling rocks (Marsal, 1967), the compression of drained sand (Nakata et al., 2001; Yamamuro et al., 1996; Yamamuro and Lade, 1996), the compression of elastic spheres (Sternberg and Rosenthal, 1952) and the compression of irregularly-shaped rocks (Hiramatsu and Oka, 1966). The size and shape of the larger fragments is strongly related to primary cracks (see Section 2.3), which propagate along the loading axis, and the primary direction of fragmentation.

A local coordinate system, $(\mathbf{x}', \mathbf{y}', \mathbf{z}')$, is assumed to control the implicit definition of the fragmentation pattern (see Fig. 4b). Its primary direction, $\mathbf{y}'$, is derived from the maximum change of relative velocity in the normal direction at each collision step. The change of relative velocity, $\triangle\mathbf{u}_i$, at each contact point, $\mathbf{c}_i$, is decomposed into its compressive, $\triangle\mathbf{u}_{i,c}$, and shear, $\triangle\mathbf{u}_{i,s}$, components, whereby

$$\triangle\mathbf{u}_{i,c} = \frac{\triangle\mathbf{u}_i\mathbf{r}_i}{|\mathbf{r}_i|} \tag{1}$$

and

$$\triangle\mathbf{u}_{i,s} = \triangle\mathbf{u}_i - \triangle\mathbf{u}_{i,c} \tag{2}$$

where $\mathbf{r}_i$ is the vector from the contact point $\mathbf{c}_i$ to the center of colliding body $\mathbf{o}$, defined as

$$\mathbf{r}_i = \mathbf{o} - \mathbf{c}_i. \tag{3}$$

The compressive component is computed at each contact point of the body. Its maximum corresponds to the contact point with the maximum change of relative velocity in the direction of compression, $\triangle\mathbf{u}_c^{max}$. It follows that

$$\mathbf{y}' = \triangle\mathbf{u}_c^{max} - \mathbf{o}. \tag{4}$$

In the simplest case, when there is only one contact point, it follows that $(\mathbf{x}', \mathbf{z}')$ is the plane with normal $\mathbf{y}'$ that passes through the body center, $\mathbf{o}$. For multiple contact points, the secondary direction is controlled by contact points which are neither close to, nor aligned with, the main contact point. In this case, the secondary direction is computed as follows. A subset of candidate contact points (see Fig. 4) is defined by $c_{i,c}$ for which $85° < \measuredangle(\mathbf{r_i}, \mathbf{y}') < 95°$. The contact point in $c_{i,c}$ with the maximum $\triangle\mathbf{u}_{i,c}$, is defined as $\max\{c_{i,p}\}$. It follows that

$$\mathbf{x}' = (\max\{c_{i,c}\} - \mathbf{o}) \times \mathbf{y}' \tag{5}$$

and

$$\mathbf{z}' = \mathbf{x}' \times \mathbf{y}'. \tag{6}$$

The primary direction $\mathbf{y}'$ is used to establish the local coordinate system for fragmentation. The detection of the primary direction is summarized in Algorithm 1. If a contact is near the primary direction, its influence should decrease, and fragmentation is set to be dominated by the primary fragment location. By applying the proposed algorithm, the secondary contact is ensured to be far from the selected primary contact. By applying the structured domain decomposition, fracture is restricted to the orthogonal system defined by the primary and secondary contacts.

Algorithm 1 Search for the primary direction

Require: A set of contact points $c_i \in \{c_0, c_1, ...c_m\}$

1: Initialize the maximum change of relative velocity in compression $\triangle \mathbf{u}_c^{max} = 0$.
2: **for** all c_i **do**
3: Calculate the change of relative velocity in compression, $\triangle \mathbf{u}_{i,c}$ using Eq. (1).
4: **If**($\triangle \mathbf{u}_{i,c} > \triangle \mathbf{u}_c^{max}$)
5: $\triangle \mathbf{u}_c^{max} = \triangle \mathbf{u}_{i,c}$
6: Calculate $\mathbf{r}_i$ using Eq. (3).
7: Set $\mathbf{r}_i$ as the primary direction, $\mathbf{y}' = \mathbf{r}_i$.
8: **End if**
9: **end for**

3.4. Structured Domain Decomposition (SDD)

The subdivision of the domain is defined implicitly by a set of seeding parameters, S, relative to the local coordinate system. A placement strategy defines the location and density of the seeds. The structured domain decomposition is subdivided into two regions, oriented by the local coordinate system. These domains are used to map original fragment elements into the post-fragmentation domains. This mapping can be performed in constant time, in the sense that its computational cost does not scale with the refinement of the original fragment. Therefore, it constitutes a low-cost fragmentation approach that trades the accuracy of a physical simulation for the speed of an empirical approach based on consistent size and shape distributions on a fragment-by-fragment basis.

The proposed approach proposes dividing the fragment domain into two regions, one local to the primary contact point, S_l, and one remote, S_r. Seeds are placed differently in S_l and S_r, allowing for the density to vary as a function of proximity to the contact. Each region is defined by a set of seeding parameters. Seeds can be placed on a structured grid, or on an alternative unstructured grid, such as a subset of the fragment discretization, or as a Voronoi mesh. In this study, $S_l = f(d_{c_{i,p}}, \Delta x', \Delta y', \Delta z')$ and $S_r = f(d_{c_{i,p}}, \Delta x', \Delta y')$ are assumed to be orthogonal domains, which subdivide the body as a function of the local coordinate system of the primary contact, and as a function of the distance to the primary contact, $d_{c_{i,p}}$. Thus, seeds are equally spaced, and placed on the orthogonal grid (x', y', z'). As a result, S_l decomposition generates denser seed placement around the contact region yielding more small fragments close to the primary contact, while S_r generates fewer larger elongated fragments away from the contact.

3.5. Error

For a given relative velocity and collision pattern, a specific structured domain decomposition is applied to fragment the body. The goal is to obtain a fragment size distribution that matches the predicted velocity-dependent Weibull parameters; this is referred to as the target distribution, $f_w^e(l)$. When the decomposition is applied, the resulting distribution is referred to as the pattern-based Weibull distribution, $f_w^p(l)$. The target function, which is the error

between fragmentation pattern-based Weibull distribution and the target Weibull distribution ε, can be expressed as

$$\varepsilon = \int_0^{l_{max}} |f_w^p(l) - f_w^e(l)| dl \tag{7}$$

The computation of seeding parameters, $S(f_w^p(l))$, for domain decomposition is based on the minimization of ε. For a given impact velocity, seeding parameters are computed iteratively. For a given impact velocity, two exact parameters of the target Weibull distribution, x_c and m, are derived. Seeding parameters are defined empirically and are applied to the original fragment geometry to generate the new fragmented geometry in constant time. The Weibull distribution is subsequently used to fit the cumulative fragment volume size distribution using a least-squares fit. The fitting error is computed based on Equation 7. If ε is below a defined threshold, the seeding parameters, $S(f_w^p(l))$ for impact velocity are tabulated (Table 3). If the error is above the threshold, the parameters are adjusted and seeding parameters are regenerated.

3.6. Seed-based fragmentation

A nominal characterization of the fragmentation pattern due to impact assumes that a primary direction axis exists during the fragmentation process. As observed experimentally, fragments can be classified into a small number of larger fragments, and a large number of smaller fragments. Smaller fragments are mainly distributed in the region close to the contact point. The size and number of smaller and larger fragments are characterized by a Weibull distribution, the parameters of which depend on contact velocity (Cheong et al., 2004; Wu et al., 2004).

A velocity-based fragmentation pattern is defined with respect to a coordinate system local to the primary contact, $c_{i,p}$, of the body (see Fig. 4). For a given impact velocity, v, fragmentation parameters can be tabulated (see Table 3), and fragmentation patterns can be *applied* to the current rock body in constant time. Fragmentation is applied to the bodies sequentially, in the same order as collisions are solved. The relationship between a given impact velocity and the three parameters of the fragmentation pattern is established using experimental results (Cheong et al., 2004; Wu et al., 2004) and numerical models which explicitly grow fractures (Paluszny et al., 2013) (see Fig. 5), or which model fragmentation as a result of sequential de-bonding of a particulate body (Wittel et al., 2008). The definition of $S(f_w^p(l))$ depends on the implementation of the method. It defines the distribution of seeds within the fragment so that the fragmentation pattern is applied. In this paper, it is proposed that $S(f_w^p(l)) = S(\Delta x' = x_s, \Delta y' = y_s, \Delta z' = z_s)$ where p_s is the number of orthogonal subdivisions in the p plane. An alternative approach would define $S(f_w^p(l))$ as a seed distribution for a 3D Voronoi subdivision of space. However, most Voronoi tesselators require decomposed domains to be convex, which cannot be guaranteed in the case of multiple-object fragmentation.

3.7. Velocity-dependent distribution of fragment sizes

Brown and Wohletz (Brown and Wohletz, 1995) showed that the Weibull distribution, which naturally occurs in fragmenting particle systems, can be derived from the physically-based Rosin-Rammler distribution that is used to

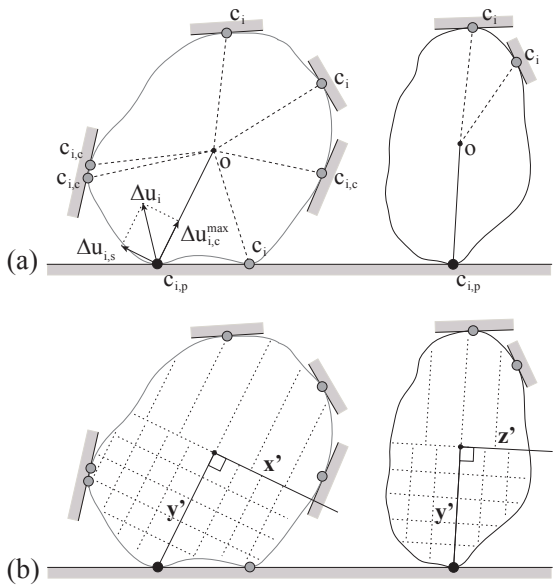


Figure 4: Contact distribution and seed placement. (a) Local coordinate system at the primary contact, $c_{i,p}$. **o** is the geometry center of the colliding body. y' is the primary axis of fragmentation, x' is the secondary axis, and z' is orthogonal to both x' and y'. Δu_i is the change of relative velocity at contact point i. $\Delta u_{i,s}$ and $\Delta u_{i,c}$ are the shearing and compression component of Δu_i, respectively. (b) Seed placement on a structured grid aligned with the local coordinate system. In (a) $S_l(4,2,2)$ and $S_r(4,2,1)$.

describe the size distribution of sequentially fragmented particulates of geological origin. The distribution equation is defined as (Weibull, 1951)

$$y = 1 - \exp\left[-\left(\frac{x}{x_c}\right)^m\right] \tag{8}$$

where x is the fragment size and $y(x)$ gives the total volume fraction corresponding to fragment sizes less than x, and m and x_c are the Weibull parameters. Larger values of m correspond to narrower distributions and vice versa (Shih, 1980), whereas x_c is the fragment size that corresponds to a volume-fraction of 1-1/e (Cheong et al., 2004). Both can be measured from experiments (Antonyuk et al., 2006) carried out for a range of impact velocities (see Fig. 6 and Fig. 7) (Cheong et al., 2004). Furthermore, Weibull parameters for specific material properties, scale, and velocity, can be approximated using forward numerical models, such as FEM/DEM fracture-driven fragmentation (Paluszny et al., 2013) or DEM fragmentation based on particle de-bonding (Wittel et al., 2008). Figures 6 and 7 compile a range experimental and numerical Weibull parameters as a function of impact velocity. Experiments reported therein refer to the fragmentation of a brittle object of $\varnothing$16mm, with a variety of geomechanical properties consistent with brittle rocks.

The target Weibull distribution, $f_w^e(l)$, where l is the size of maximum resulting fragment, is interpolated from experimental data and depends on fragment size and collision velocity. By applying the seeding parameters to the colliding body, a set of new sub-fragments are obtained that follow a two-parameter pattern-based Weibull distribution of sizes, $f_w^p(l)$. The parameters of the structured domain decomposition (see Section 3.4) are assigned by minimizing the

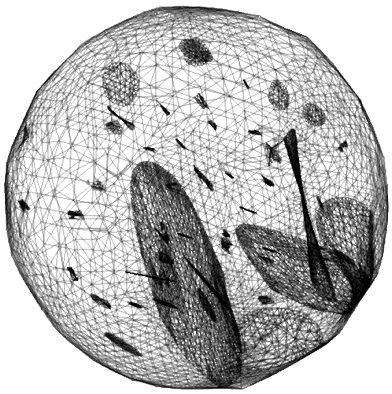


Figure 5: FEM/DEM modeling of fracture-driven fragmentation (Paluszny et al., 2013). Fractures are propagated within each fragment using a velocity-dependent Paris propagation law which controls the relative velocity of fractures. These simulations generate fragment size distributions which conform with the expected Weibull distribution.

difference between $f_w^e(l)$ and $f_w^p(l)$. The process aims to minimize the difference between the target and pattern-based distributions by iteratively adjusting the seeding parameters, as follows:

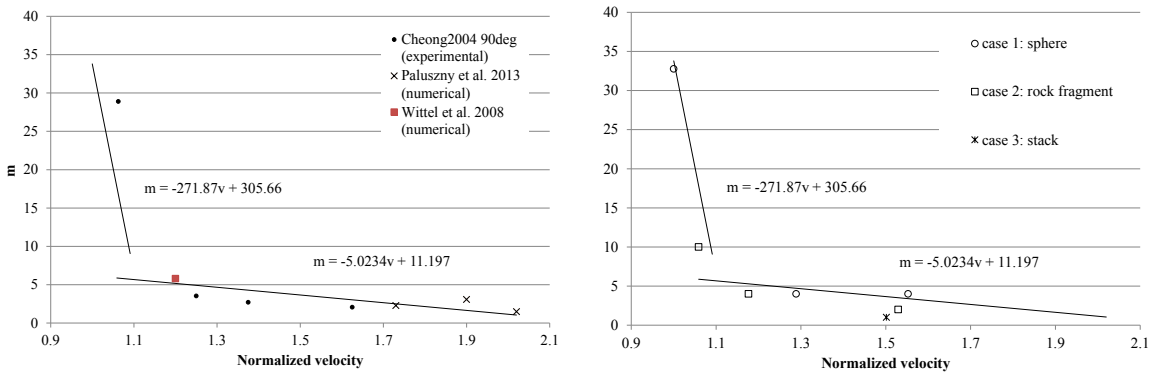
1. Compute velocity dependent Weibull distribution parameters, m and x_c
2. Iteratively compute structured domain decomposition
3. Fragment body
4. Compute volume-based cumulative fragmentation size
5. Compute error and refine seeding

Finally, rock fragment elements are classified into new sub-fragments, following the fragmentation pattern derived from the seeding iteration. The geometry of the colliding bodies is updated, and the dynamics simulator updates the contact forces between the fragments. The new fragments are then assigned consistent post-impact velocities. The relationship between impact velocities and structured domain decomposition is derived from existing physical and numerical experiments. This iteration could be extended to account for internal impacts between fragments during the fragmentation (Vocialta and Molinari, 2015) by adding a dynamics step to the seeding parameters adjustment loop.

4. Case study

4.1. Fragmentation of a single sphere

The performance of the fragmentation pattern is validated by modeling the fragmentation of a single sphere, $\varnothing$12.7 mm. Density is assumed to be 2750 kg/m^3. The sphere is discretized with 550 tetrahedra. The restitution coefficient is zero, and friction is ignored. The sphere falls downwards and collides with a rigid ground at impact velocities of 17 m/s, 20 m/s, and 26 m/s; these velocities are chosen to match available experimental results.



(a) (b)

Figure 6: Experimental relation between impact velocity and parameter m of the Weibull distribution: (a) experimental and numerical values, and (b) predicted values using the present method.

Relative velocities are zero after the collision, and absolute values of the change of the relative velocities and impact velocities remain unchanged. For an impact velocity of 17 m/s, according to Table 3, the closest tabulated velocity is 16.66 m/s and the parameters of the fragmentation pattern are estimated as $S(3, 2, 2)$. For an impact velocity of 20 m/s, velocity and seeding parameters are approximated as 21.47 m/s and $S(3, 4, 3)$. For an impact velocity of 26 m/s, the best match velocity is 26.26 m/s and the seeding parameters are $S(6, 60, 6)$. Figure 8 shows the resulting fragment shapes.

Figure 9 shows the shape of the fragments resulting from direct fragmentation at impact velocities of (a) 20 m/s and (b) 26 m/s. The number of fragments increases with increasing impact velocity (Fig. 9 (c)). Once the impact velocity reaches 26 m/s, the region around the contact points is fragmented into a large number of small fragments. The rest of the sphere is fragmented into several main fragments. This distribution of small and main fragments is in agreement with the experimental observations in (Cheong et al., 2004).

The two-parameter Weibull distribution equation is then used to fit the cumulative fragment (volume) size distribution, by a least-squares fit. In Fig. 9, the size distributions obtained from the simulation are marked by circles, regular triangles and inverted triangles, for impact velocities of 17 m/s, 20 m/s, and 26 m/s, respectively.

4.2. Fragmentation of an irregularly shaped rock

A $3 \times 4 \times 5$ m irregularly-shaped rock is compressed by a falling cuboid hammer. The shape is a simplified discretization of an actual scanned rock. A total of 1458 tetrahedral elements are used to discretize the body (see Fig. 10).

As for the previous case, three impact velocities are considered: 17 m/s, 20 m/s, and 26 m/s. The restitution coefficient and friction coefficient are both zero; therefore, relative velocities are zero after collision, and the absolute of initial impact velocities equals the change of relative velocities. At the onset of the collision, the impacted body

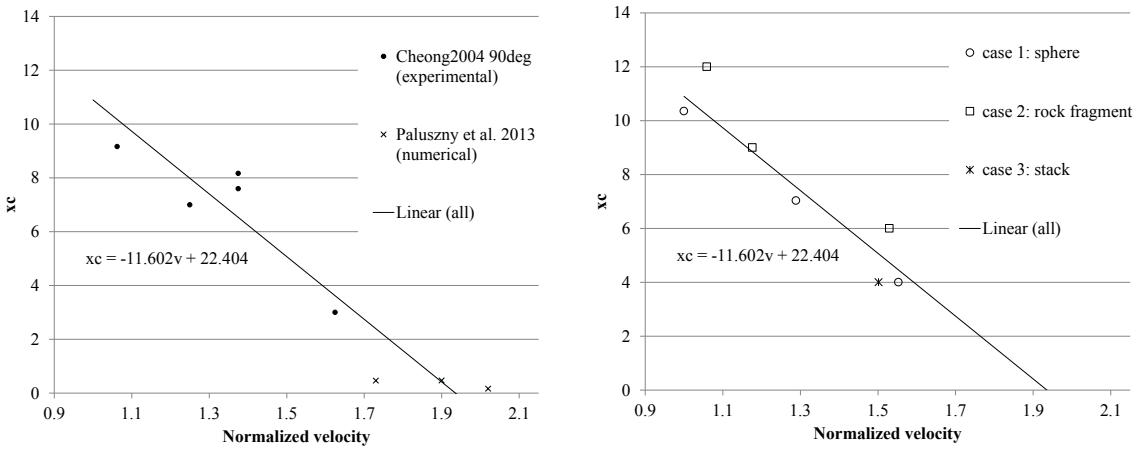


Figure 7: Experimental relation between impact velocity and parameter x_c of the Weibull distribution: (a) experimental and numerical values, and (b) predicted values using the present method.

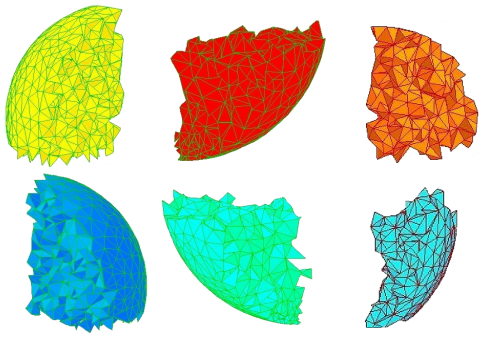


Figure 8: Shape of fragments resulting from the direct fragmentation of a single sphere.

is fragmented using the same seeding parameters as for the spherical case. After the initial impact, subsequent fragmentation patterns are applied as a function of the local velocity of individual fragments that result during the simulation. Fragmentation is progressive, and for the highest velocity the impact results in complete shattering of the rock.

The rock is fragmented into a number of smaller fragments, and several larger fragments, apparent in Fig. 11 and highlighted in Fig. 12. The discretization of the fragment does not change during fragmentation. Smaller fragments are mostly distributed in the vicinity of the contacts. A similar distribution of smaller fragments and larger fragments are observed as in experiments of the fragmentation of a single sphere. A two-parameter Weibull distribution illustrates the final volume cumulative fragment size distribution of fragments (Fig. 12).

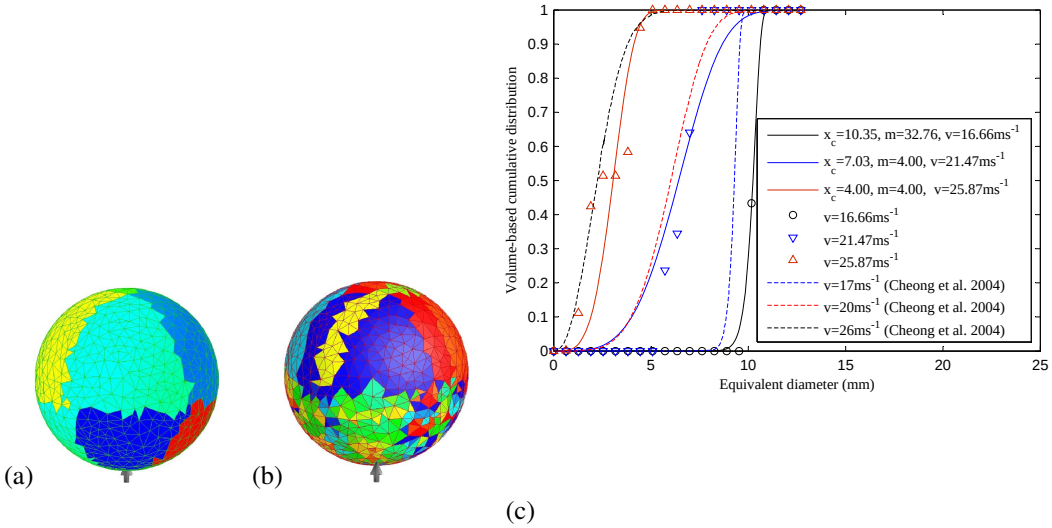


Figure 9: Shape of fragments from the direct fragmentation of a single sphere with impact velocities (a) 17 m/s and (b) 26 m/s. Fragments are colored arbitrarily to distinguish them from each other. (c) Volume cumulative size distribution resulting from the fragmentation fitted by a two-parameter Weibull distribution equation.

4.3. Case study: Fragmentation of a stack of spheres

Fragmentation is modeled here in the context of high pressure grinding rolls, used to comminute ore particles. Studying confined multiple particle breakage is critical to reduce comminution energy and enhance downstream mineral recover in pressure grinding rolls (Ali and Bradshaw, 2011).

This test investigates breakage of a confined particle bed, which consists of $5 \times 5 \times 5$ ore particles. These ore particles are placed in a static and rigid container, which has static and rigid boundary walls on five sides, as shown in Fig. 13. A $60 \times 60 \times 25$ m cuboid hammer moves downwards and compresses the ore particles. The dimensions of the container are $60 \times 60 \times 110$ m. The height, width and length of the particle bed are all 60 m. The ore particles are spherical, and their diameter is 12 m. Each sphere is discretized using 550 tetrahedra, so that the total number of elements used to discretize the spheres is 68,750. The container is discretized using 4025 tetrahedral elements, and the hammer is discretized by six large tetrahedral elements. Note that the container need not be finely meshed to match sphere refinement, as is required in other approaches.

The restitution coefficient and friction coefficient of the ore particles are set to 0.8 and 0.4, and for the container and hammer, 0.7 and 0.4, respectively. To study the influence of the crushing velocity, two tests, DC1f and DC2f are conducted. In DC1f, the crushing velocity is 10 m/s, and in DC2f, the crushing velocity is 100 m/s (Fig. 14 and 15). For a crushing velocity of 10 m/s, the hammer starts to compress the ore particles at step 598. For impact velocity of 100 m/s, the first collision between the hammer and ore particles is detected at step 541. Before the hammer hits the particles, step advance is controlled by particle interaction within the container.

Fragmentation develops from the top of the ore particles to the bottom as the simulation progresses. For both

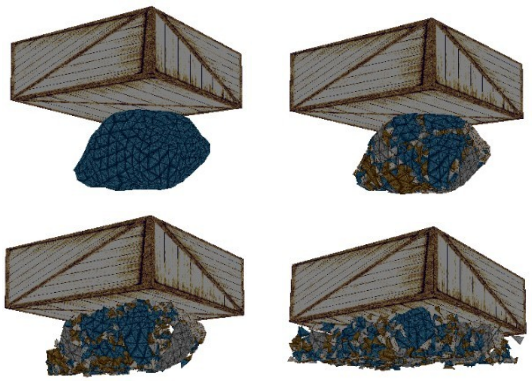


Figure 10: Progressive fragmentation sequence for crushing of an irregularly-shaped rock block, with an initial crushing velocity of 26 m/s.

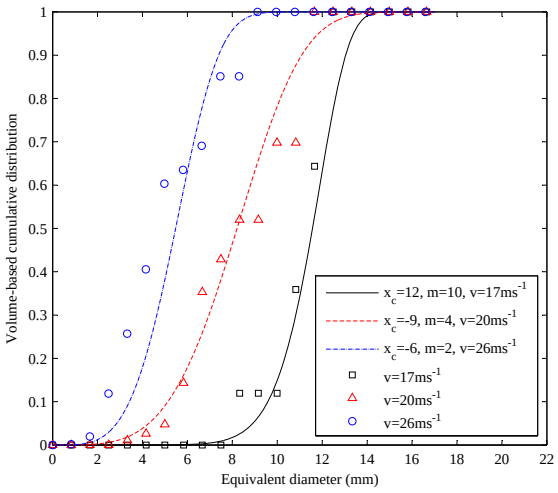


Figure 11: Cumulative volumetric size distribution of fragments from fragmentation process depicted in Figure 10.

DC1f and DC2f, most damage occurs in the upper layers. The size distribution of ore particles of DC1f at step 658 and the size distribution of ore particles of DC2f at step 650 are plotted in Fig. 14 and 15, respectively. The x axis is the normalized fragmentation volume, and the y axis it the percent of total volume. The Weibull distribution fits the size distribution of crushed the fragments, whose volume is smaller than the original volume, 868 m^3. The size distributions in DC1f and DC2f are similar, even the number of damage fragments increase significantly with the increase of crushing velocity. Fragmentation increases with the increase of impact velocities. For instance, for DC2f, the crushing velocity is 10 m/s, and approximately 43% of fragments are smaller than 600 m^3. For DC1f, the crushing velocity is 100 m/s, and approximately 18% of the fragments are smaller than 600 m^3. If 600 m^3 is the maximum limit to collect ore fragments, the amount of qualified ore fragments produced in DC1f is 25% more than in DC2f. These observations agree with physical and numerical experiments that show catastrophic damage to the top-layered ore particles of an initially intact bed (Ali and Bradshaw, 2011; Khanal et al., 2007; Liu et al., 2005; Tsoungui et al., 1999).

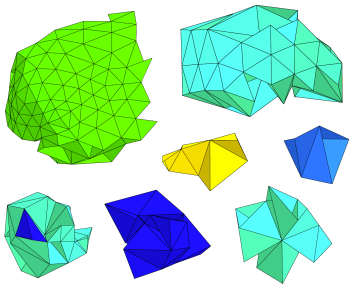


Figure 12: Realistic shape rock. Shapes of the created fragments.

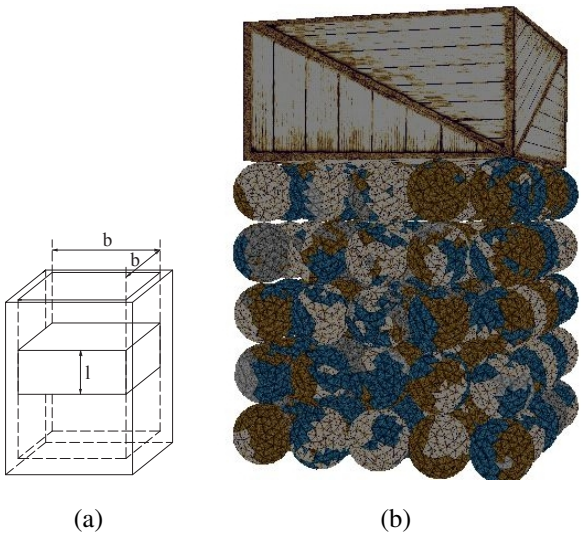


Figure 13: Geometry of container and fragment pattern. (a) The dimension of the container is $b \times b$, where b=6cm. The depth of the hammer is l=25 m. (b) Fragment distribution after impact for DCf2 colored by particle.

The total computational time of each simulation step increases significantly with the increase in the number of contacts. More fragments are generated in DC2f (v=100 m/s) than in DC1f (v=10 m/s); therefore, the total computational time of each simulation step increases more in DC2f than does the total computational time of each simulation step in DC1f. Total computational time and the number of contacts at each simulation step increase linearly (Fig. 16). However, the cost of fragmentation does not significantly increase with the increase of number of contacts, even though average computational time per contact increases with the increase of number of contacts.

5. Conclusions

A low-cost fragmentation pattern based approach is proposed to model the fragmentation of colliding bodies. Colliding bodies are fragmented directly, without simulating de-bonding or crack propagation, thereby avoiding

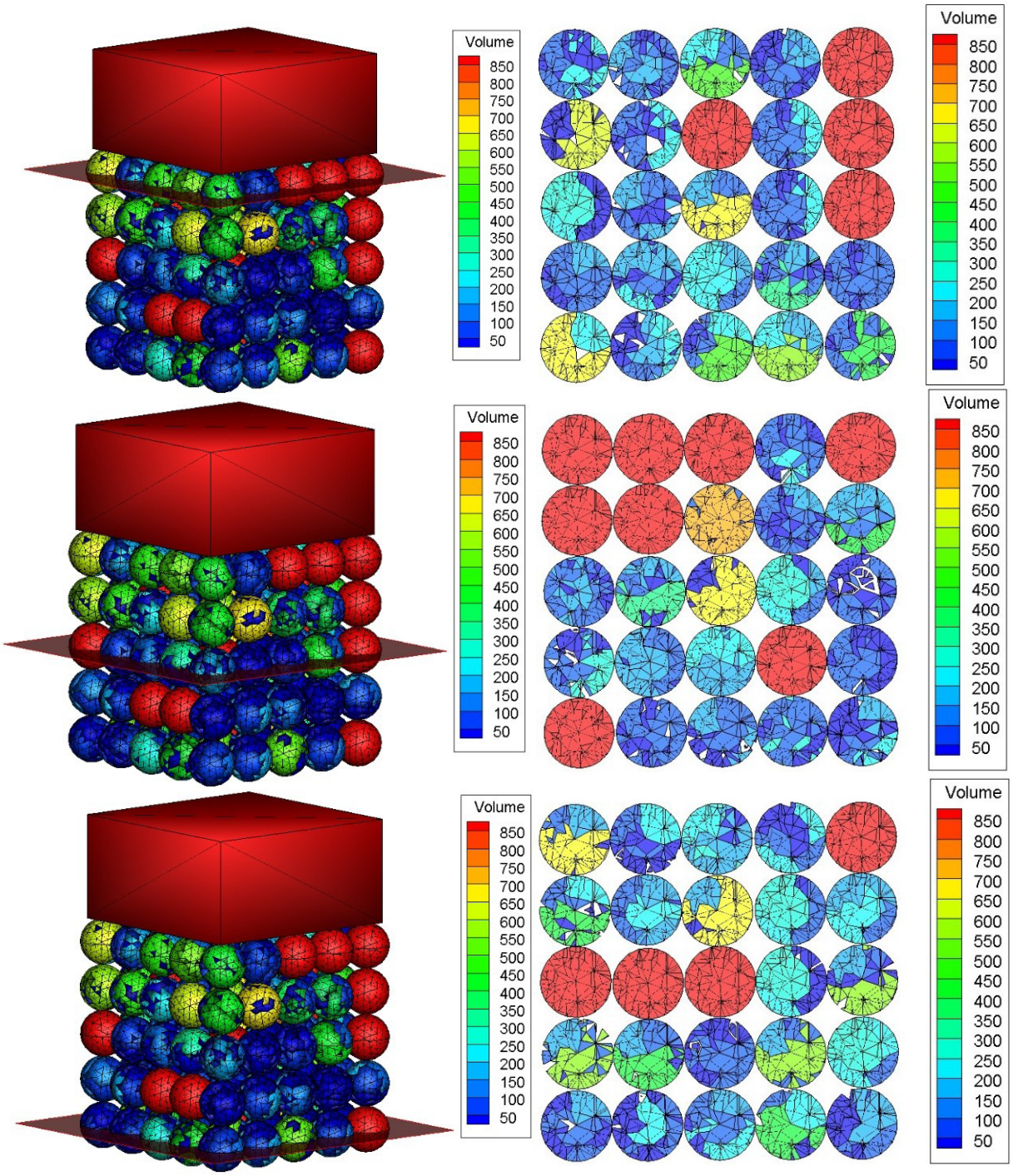


Figure 14: Fragment distribution after impact for DCf1 colored by particle volume. Intact ore particles, of volume 868 m^3, are colored in orange and smaller ore fragments, of volume less than 200 m^3, are in blue.

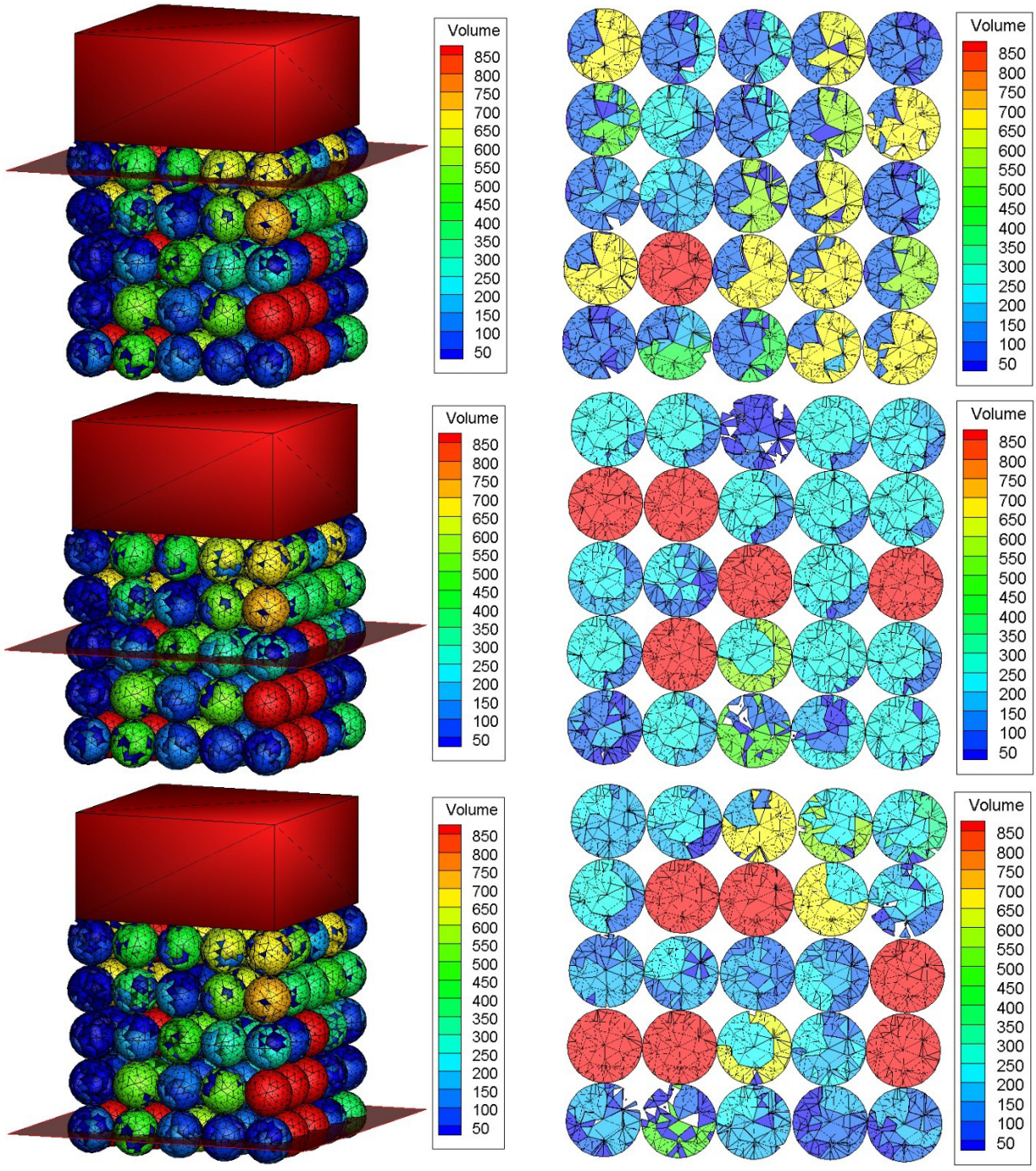


Figure 15: Fragment distribution after impact for DCf2 colored by particle volume. Intact ore particles, of volume 868 m^3, are colored in orange and smaller ore fragments, of volume less than 200 m^3, are in blue.

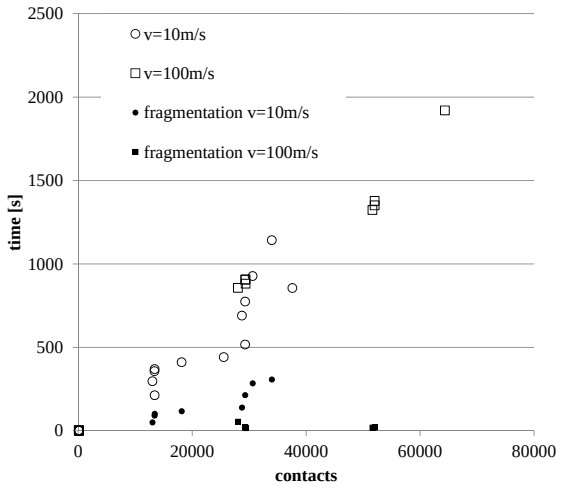


Figure 16: Total computation time and computational time of fragmentation per number of contacts at each simulation step for crushing velocities of v=10 m/s and v=100 m/s.

re-meshing and re-creating the solid geometry during the simulation. However, applied fragmentation patterns are based on experimental observations and numerical experiments of fracture-driven fragmentation. Fragmentation patterns are controlled by a structural domain decomposition dependent on the relative impact velocities, and final fragment size volume-based cumulative distributions follow physically-based Weibull distributions.

The presented method reduces computational cost substantially, as it is applied as a pattern to the colliding body, and avoids iteratively updating the geometry. The method does not change or increase the number of elements of the colliding bodies due to fragmentation, ensuring geometric robustness of the simulation. The fragmentation pattern is informed by existing, shape, material and size-specific experimental and numerical results. The method ensures the creation of fragment size distributions that are consistent with high-resolution simulations in which resulting fragment sizes follow a two-parameter Weibull distribution. As opposed to a purely stochastic method, this new method takes into account the geometry of the contacts, and the spatial relation and magnitude of the compressive velocities at each contact. It applies fragmentation patterns that relate a distribution of sizes consistent with the local distribution of the contacts of each fragment.

The presented method is simple, and ignores many factors that influence fragmentation, such as pre-existing cracks and material heterogeneities. However, it presents a low-cost approach to incorporating fragmentation into DEM simulations in constant time, while generating realistic fragment shape distributions.

6. Acknowledgments

The authors thank Rio Tinto for supporting this work, through the Rio Tinto Centre for Advanced Mineral Recovery at Imperial College London. They also thank the European Commission for partially funding this work through the

TRUST Collaborative Project, 309067.

References

Ali, A., Bradshaw, S., 2011. Confined particle bed breakage of microwave treated and untreated ores. Minerals Engineering 24 (14), 1625–1630.

Andrews, E., Kim, K., 1999. Threshold conditions for dynamic fragmentation of glass particles. Mechanics of Materials 31, 689–703.

Antonyuk, S., Khanal, M., Tomas, J., Heinrich, S., Mörl, L., 2006. Impact breakage of spherical granules: Experimental study and DEM simulation. Chemical Engineering and Processing: Process Intensification 45, 838–856.

Arbiter, N., Harris, C., Stamboltzis, G., 1969. Single fracture in brittle spheres. Transactions of the AIME 244, 118–133.

Åström, J., 2006. Statistical models of brittle fragmentation. Advances in Physics 55, 247–278.

Åström, J., Holian, B., Timonen, J., 2000. Universality in Fragmentation. Physical Review Letters 84, 3061–3064.

Åstrom, J., Ouchterlony, F., Linna, R., Timonen, J., 2004. Universal dynamic fragmentation in D dimensions. Physical Review Letters 92, 245506–1.

Banerjee, B., June 2004. Material point method simulations of fragmenting cylinders. In: 17th ASCE Engineering Mechanics Conference. University of Delaware, Newark, USA, p. 1.

Behera, B., Kun, F., McNamara, S., Herrmann, H., 2005. Fragmentation of a circular disc by projectiles. Journal of Physics: Condensed Matter 17, S2439–S2456.

Belytschko, T., Black, T., 1999. Elastic crack growth in finite elements with minimal remeshing. International Journal for Numerical Methods in Engineering 45, 601–620.

Belytschko, T., Lu, Y., Gu, L., 1994. Element-free galerkin methods. International Journal for Numerical Methods in Engineering 37 (2), 229–256.

Brown, W. K., Wohletz, K. H., 1995. Derivation of the Weibull distribution based on physical principles and its connection to the Rosin-Rammler and lognormal distributions. Journal of Applied Physics 78 (4), 2758–2763.

Bruchmüller, J., van Wachem, B., Gu, S., Luo, K., 2011. Modelling discrete fragmentation of brittle particles. Powder Technology 208, 731–739.

Camacho, G., Ortiz, M., 1996. Computational modelling of impact damage in brittle materials. International Journal of Solids and Structures 33 (20-22), 2899 – 2938.

Carmona, H., Wittel, F., Kun, F., Herrmann, H., 2008. Fragmentation processes in impact of spheres. Physical Review E - Statistical, Nonlinear, and Soft Matter Physics 77, 1–10.

Chau, K., Wei, X., Wong, R., Yu, T., 2000. Fragmentation of brittle spheres under static and dynamic compressions: Experiments and analyses. Mechanics of Materials 32, 543–554.

Cheong, Y., Reynolds, G., Salman, A., Hounslow, M., 2004. Modelling fragment size distribution using two-parameter Weibull equation. International Journal of Mineral Processing 74 (0), S227–S237.

Cheong, Y., Salman, A., Hounslow, M., 2003. Effect of impact angle and velocity on the fragment size distribution of glass spheres. Powder Technology 138, 189–200.

Cundall, P. A., Strack, O. D. L., 1979. A discrete numerical model for granular assemblies. Geotechnique 29, 47–65.

Daux, C., Moes, N., Dolbow, J., Sukumar, N., Belytschko, T., 2000. Arbitrary branched and intersecting cracks with the extended finite element method. International Journal for Numerical Methods in Engineering 48(12), 1741–1760.

Djordjevic, N., Morrison, R., 2006. Exploratory modelling of grinding pressure within a compressed particle bed. Minerals Engineering 19 (10), 995 – 1004.

Doyoyo, M., 2002. A theory of the densification-induced fragmentation in glasses and ceramics under dynamic compression. International Journal of Solids and Structures 39, 1833–1843.

Giacomini, A., Buzzi, O., Renard, B., Giani, G., 2009. Experimental studies on fragmentation of rock falls on impact with rock surfaces. International Journal of Rock Mechanics and Mining Sciences 46 (4), 708–715.

Gilvarry, J., Bergstorm, B., 1961. Fracture of brittle solids. ii. distribution function for fragment size in a single fracture (experimental). Journal of Applied Physics 32, 400–410.

Gorham, D., Salman, A., 2005. The failure of spherical particles under impact. Wear 258 (1-4), 580–587.

Gorham, D., Salman, A., Pitt, M., 2003. Static and dynamic failure of PMMA spheres. Powder Technology 138, 229–238.

Grady, D., 2010. Length scales and size distributions in dynamic fragmentation. International Journal of Fracture 163, 85–99.

Grange, S., Forquin, P., Mencacci, S., Hild, F., 2008. On the dynamic fragmentation of two limestones using edge-on impact tests. International Journal of Impact Engineering 35, 977–991.

Hiramatsu, Y., Oka, Y., 1966. Determination of the tensile strength of rock by a compression test of as irregular test piece. International Journal of Rock Mechanics and Mining Sciences 3, 89–99.

Holl, M., Rogge, T., Loehnert, S., Wriggers, P., Rolfes, R., 2014. 3d multiscale crack propagation using the XFEM applied to a gas turbine blade. Computational Mechanics 53 (1), 173–188.

Holland, M., Urai, J., Martel, S., 2006. The internal structure of fault zones in basaltic sequences. Earth and Planetary Science Letters 248 (1-2), 301.

Inaoka, H., Takayasu, H., 1996. Universal fragment size distribution in a numerical model of impact fracture. Physica A: Statistical and Theoretical Physics 229, 5–25.

Kafui, K., Thornton, C., 2000. Numerical simulations of impact breakage of a spherical crystalline agglomerate. Powder Technology 109, 113–132.

Khanal, M., Schubert, W., Tomas, J., 2004. Ball impact and crack propagation - simulations of particle compound material. Granular Matter 5, 177–184.

Khanal, M., Schubert, W., Tomas, J., 2007. Discrete element method simulation of bed comminution. Minerals Engineering 20, 179–187.

Khanal, M., Schubert, W., Tomas, J., 2008. Compression and impact loading experiments of high strength spherical composites. International Journal of Mineral Processing 86, 104–113.

Kun, F., Herrmann, H., 1998. Transition from damage to fragmentation in collision of solids. Physical Review E 59 (3), 2623–2632.

Kuna, F., Herrmann, H., 1996. A study of fragmentation processes using a discrete element method. Computer Methods in Applied Mechanics and Engineering 138, 3–18.

Kutter, H., Fairhurst, C., 1971. On the fracture process in blasting. International Journal of Rock Mechanics and Mining Sciences & Geomechanics Abstracts 8, 181–202.

Lai, X., Ren, B., Fan, H., Li, S., Wu, C., Regueiro, R. A., Liu, L., 2015. Peridynamics simulations of geomaterial fragmentation by impulse loads. International Journal for Numerical and Analytical Methods in Geomechanics 39 (12), 1304–1330.

Lee, K., Farhoomand, I., 1997. Compressibility and crushing of granular soils in aisotropic triaxial compression. Canadian Geotechnical Journal 4 (1), 68–86.

Libersky, L. D., Randles, P. W., Carney, T. C., Dickinson, D. L., 1997. Recent improvements in {SPH} modeling of hypervelocity impact. International Journal of Impact Engineering 20 (6-10), 525–532.

Lin, M., Canny, J., April 1991. A fast algorithm for incremental distance calculation. In: Proceeding of the IEEE International Conference on Robotics and Automation, IEEE. Sacramento, CA , USA, p. 1.

Linna, R., Å ström, J., Timonen, J., 2005. Dimensional effects in dynamic fragmentation of brittle materials. Physical Review E - Statistical, Nonlinear, and Soft Matter Physics 72, 1–4.

Liu, H., Kou, S., Lindqvist, P., 2005. Numerical studies on the inter-particle breakage of a confined particle assembly in rock crushing. Mechanics of Materials 37, 935–954.

Lu, C., Danzer, R., Fischer, F., 2002a. Fracture statistics of brittle materials: Weibull or normal distribution. Physical Review E - Statistical, Nonlinear, and Soft Matter Physics 65, 1–4.

Lu, C., Danzer, R., Fischer, F. D., Jun 2002b. Fracture statistics of brittle materials: Weibull or normal distribution. Physical Review E 65, 067102.

Majzoub, R., Chaudhri, M., 2000. High-speed photography of low-velocity impact cracking of solid spheres. Philosophical Magazine Letters 80, 387–393.

Marsal, R., 1967. Large scale testing of rockfill materials. Journal of Soil Mechanics and Foundations Division ASCE 93 (2), 27–43.

Maxim, R., Salman, A., Hounslow, M., 2006. Predicting dynamic failure of dense granules from static compression tests. International Journal of Mineral Processing 79, 188–197.

Meibom, A., Balslev, I., 1996. Composite Power Laws in Shock Fragmentation. Physical Review Letters 76 (14), 2492–2494.

Mesri, G., Vardhanabhutib, B., 2009. Compression of granular materials. Canadian Geotechnical Journal 46 (4), 369–392.

Mirtich, B., Canny, J., 1995. Impulse-based simulation of rigid bodies. In: Proceedings of the 1995 Symposium on Interactive 3D Graphics. I3D '95. ACM, New York, NY, USA, pp. 181–217.

Mishra, B., Thornton, C., 2001. Impact breakage of particle agglomerates. International Journal of Mineral Processing 61, 225–239.

Munjiza, A., Andrews, K., White, J., 1999. Combined single and smeared crack model in combined finite-discrete element analysis. International Journal for Numerical Methods in Engineering 44 (1), 41–57.

Munjiza, A., Knight, E., Rougier, E., 2011. Computational Mechanics of Discontinua. Wiley.

Munjiza, A., Latham, J. P., Andrews, K. R. F., 2000. Detonation gas model for combined finite-discrete element simulation of fracture and fragmentation. International Journal for Numerical Methods in Engineering 49 (12), 1495–1520.

Munjiza, A., Owen, D., Bicanic, N., 1995. A combined finite-discrete element method in transient dynamics of fracturing solids. Engineering Computations 12 (2), 145–174.

Nakata, Y., Hyodo, M., andY. Kato, A. H., Murata, H., 2001. Microscopic particle crushing and sand subjected to one-dimensional compression. Soils and Foundations 41 (1), 69–82.

Oddershede, L., Dimon, P., Bohr, J., 1993. Self-organized criticality in fragmenting. Physical Review Letters 71 (19), 3107–3110.

Paluszny, A., Tang, X. H., Zimmerman, R. W., 2013. A fracture- and impulse-based FDEM approach for fragmentation. Computational Mechanics 52 (5), 1071–1084.

Paluszny, A., Zimmerman, R. W., 2011. Numerical simulation of multiple 3D fracture propagation using arbitrary meshes. Computer Methods in Applied Mechanics and Engineering 200 (9-12), 953–966.

Paluszny, A., Zimmerman, R. W., 2013. Numerical fracture growth modeling using smooth surface geometric deformation. Engineering Fracture Mechanics 108, 19–36.

Potapov, A., Campbell, C., 1994. Computer simulation of impact-induced particle breakage. Powder Technology 81, 207–216.

Potapov, A., Campbell, C., 1997. The two mechanisms of particle impact breakage and the velocity effect. Powder Technology 93, 13–21.

Potapov, A., Campbell, C., 2001. Parametric dependence of particle breakage mechanisms. Powder Technology 120, 164–174.

Rabczuk, T., Areias, P., Belytschko, T., 2007. A simplified mesh-free method for shear bands with cohesive surfaces. International Journal for Numerical Methods in Engineering 69, 993–1021.

Rabczuk, T., Belytschko, T., 2004. Cracking particles: a simplified meshfree method for arbitrary evolving cracks. International Journal for Numerical Methods in Engineering 61 (13), 2316–2343.

Rabczuk, T., Belytschko, T., Xiao, S., 2004. Stable particle methods based on lagrangian kernels. Computer Methods in Applied Mechanics and Engineering 193 (26), 1035–1063.

Rabczuk, T., Eibl, J., 2003. Simulation of high velocity concrete fragmentation using sph/mlsph. International Journal for Numerical Methods in Engineering 56 (10), 1421–1444.

Ren, B., Li, S., 2010. Meshfree simulations of plugging failures in high-speed impacts. Computers and Structures 88 (15-16), 909–923.

Ren, B., Li, S., 2012. Modeling and simulation of large-scale ductile fracture in plates and shells. International Journal of Solids and Structures 49 (18), 2373–2393.

Riou, P., Denoual, C., Cottenot, C., 1998. Visualization of the damage evolution in impacted silicon carbide ceramics. International Journal of Impact Engineering 21 (4), 225–235.

Salman, A., Biggs, C., Fu, J., Angyal, I., Szabó, M., Hounslow, M., 2002. An experimental investigation of particle fragmentation using single particle impact studies. Powder Technology 128, 36–46.

Salman, A., Gorham, D., 2000. The fracture of glass spheres. Powder Technology 107, 179–185.

Salman, A., Gorham, D., Verba, A., 1995. A study of solid particle failure under normal and oblique impact. Wear 186-187 (1), 92–98.

Salman, A., Reynolds, G., Fu, J., Cheong, Y., Biggs, C., Adams, M., Gorham, D., Lukenics, J., Hounslow, M., 2004. Descriptive classification of the impact failure modes of spherical particles. Powder Technology 143-144, 19–30.

Santurbano, R., Fairhurst, C., 1991. Fracture Mechanics In the Context of Rock Crushing: Preliminary Experimental Results Concerning the Impact

of Limestone Spheres. American Rock Mechanics Association, 441–450.

Schönert, K., 2004. Breakage of spheres and circular discs. Powder Technology 143-144, 2–18.

Schubert, W., Khanal, M., Tomas, J., 2005. Impact crushing of particle-particle compounds experiment and simulation. International Journal of Mineral Processing 75, 41–52.

Shih, T., 1980. An evaluation of the probabilistic approach to brittle design. Engineering Fracture Mechanics 13 (2), 257–271.

Shockey, D., Curran, D., Seaman, L., Rosenberg, J., Petersen, C., 1974. Fragmentation of rock under dynamic loads. International Journal of Rock Mechanics and Mining Sciences & Geomechanics Abstracts 11, 303–317.

Sternberg, E., Rosenthal, F., 1952. The elastic sphere under concentrated loads. Journal of Applied Mechanics 19, 413–421.

Sukumar, N., Moes, N., Moran, B., Belytschko, T., 2000. Extended finite element method for three-dimensional crack modelling. International Journal for Numerical Methods in Engineering 48, 1549–1570.

Sulsky, D., Chen, Z., Schreyer, H., 1994. A particle method for history-dependent materials. Computer Methods in Applied Mechanics and Engineering 118, 179–196.

Tang, X., Paluszny, A., Zimmerman, R., 2013a. Energy conservative property of impulse-based methods for collision resolution. International Journal for Numerical Methods in Engineering 95 (6), 529–540.

Tang, X., Paluszny, A., Zimmerman, R. W., 2014. An impulse-based energy tracking method for collision resolution. Computer Methods in Applied Mechanics and Engineering 278 (0), 160 – 185.

Tang, X. H., Paluszny, A., Zimmerman, R. W., 23-26 June 2013b. A study of the influence of fragmentation in ore-pass hang-up phenomena. In: ARMA 2013. San Francisco, USA.

Thornton, C., Ciomocos, M., Adams, M., 1999. Numerical simulations of aggolomerate impact breakage. Powder Technology 105, 74–82.

Thornton, C., Yin, K., Adams, M., 1996. Numerical simulation of the impact fracture and fragmentation of agglomerates. Journal of Physics D: Applied Physics 29, 424–435.

Tomas, J., Schreier, M., Gröger, T., Ehlers, S., 1999. Impact crushing of concrete for liberation and recycling. Powder Technology 105, 39–51.

Tromans, D., 2008. Mineral comminution: energy efficiency considerations. Minerals Engineering 21 (8), 613–620.

Tsoungui, O., Vallet, D., Charmet, J., Roux, S., 1999. Size effects in single grain fragmentation. Granular Matter 2, 19–27.

Turcotte, D., 1986. Fractals and fragmentation. Journal of Geophysical Research: Solid Earth 91 (5), 1921–1926.

Vocialta, M., Molinari, J.-F., 2015. Influence of internal impacts between fragments in dynamic brittle tensile fragmentation. International Journal of Solids and Structures 153, 247–256.

Vyazmensky, A., Elmo, D., Stead, D., 27-31 May 2007 2007. Combined finite-discrete element modelling of surface subsidence associated with block caving mining. In: Proceedings of the 1st Canada-US Rock Mechanics Symposium. Vancouver, Canada, pp. 467–475.

Wang, Y., Tonon, F., 2010. Calibration of a discrete element model for intact rock up to its peak strength. International Journal for Numerical and Analytical Methods in Geomechanics 34 (5), 447–469.

Wang, Y., Tonon, F., 2011. Discrete element modeling of rock fragmentation upon impact in rock fall analysis. Rock Mechanics and Rock Engineering 44, 23–35.

Wang, Y. N., 2009. Three-dimensional rock-fall analysis with impact fragmentation and fly-rock modelling. Ph.D. thesis, University of Texas at Austin.

Weibull, W., 1951. A statistical distribution function of wide applicability. Journal of Applied Mechanics 18, 293–296.

Wittel, F., 2010. Single particle fragmentation in ultrasound assisted impact comminution. Granular Matter 12, 447–455.

Wittel, F., Carmona, H., Kun, F., Herrmann, H., 2008. Mechanisms in impact fragmentation. International Journal of Fracture 154 (1-2), 105–117.

Wu, S., Chau, K., Yu, T., 2004. Crushing and fragmentation of brittle spheres under double impact test. Powder Technology 143-144, 41–55.

Xiang, J., Munjiza, A., Latham, J., Guises, R., 2009. On the validation of DEM and FEM/DEM models in 2D and 3D. Engineering Computations 26 (6), 673–687.

Yamamuro, J., Bopp, P., Lade, P., 1996. One-dimensional compression of sands at high pressures. Journal of Geotechnical Engineering, ASCE 122 (2), 147–154.

Yamamuro, J., Lade, P., 1996. Drained sand behaviour in axisymmetric tests at high pressures. Journal of Geotechnical Engineering, ASCE 122 (2), 109–119.

Zhang, X., Jia, G., Huang, H., 2013. Finite element reconstruction approach for on-orbit spacecraft breakup dynamics simulation and fragment analysis. Advances in Space Research 3 (1), 423–433.

Table 1: Details of physical experiments of sphere fragmentation

Research	d(mm)	v(m/s)	sample material	anvil material	angle
Drop-shatter experiments					
Arbiter et al. (1969)	74-124	0-7.6	concrete	steel	90°
Santurbano and Fairhurst (1991)	25	7-52	limestone	3.6 m long Hopkinson bar	90°
Salman et al. (1995)	5.15	40-130	aluminum oxide	5 mm thick plate of mild steel	20°-90°
Andrews and Kim (1999)	0.79-6.35	10-120	soda-lime glass, aluminum oxide, silicon nitride	25 mm thick titanium diboride	90°
Salman and Gorham (2000)	0.4-12.7	20- 120	soda-lime glass	aluminum oxide anvil	90°
Salman et al. (2002)	3.15-7.15	5-30	aluminum oxide	steel, aluminium, glass, plexiglas	10°-90°
Gorham et al. (2003)	8	40-130	PMMA	aluminum oxide	90°
Cheong et al. (2003)	1, 3, 6, 12.7	20-100	soda-lime glass	aluminum oxide	15°-90°
Cheong et al. (2004)	12.7	17- 26	soda-lime glass	aluminum oxide	15°-90°
Salman et al. (2004)	0.4-13	2.45-100	aluminum oxide, soda-lime glass, PMMA, granules	glass, high-strength ceramic and tool steel	90°
Schönert (2004)	8	85	PMMA	-	90°
Gorham and Salman (2005)	0.4-13	8-20	soda-lime glass, PMMA	high-strength sintered aluminum oxide	90°
Maxim et al. (2006)	5.3	1-20	fertilizer granules	-	10°-90°
Antonyuk et al. (2006); Schubert et al. (2005); Tomas et al. (1999)	0.8-1.76	10-50	γ-Al2O3, synthetic, zeolite Kostrolith, sodium benzoate	-	90°
Khanal et al. (2008)	150	7.7-75	concrete	-	90°
Double-impact experiments					
Chau et al. (2000)	37, 48, 59	1-3	plaster	n.a.	n.a.
Majzoub and Chaudhri (2000)	12.7	5	acrylic resin, PMMA		
Wu et al. (2004)	50, 60, 75	1-9	plaster	n.a.	n.a.

Table 2: Three dimensional discrete element method fragmentation simulations of (I) impact, (DI) double impact, and (C) compression experiments. The abbreviated 'mass dist.' and 'size dist.' stand for mass and size distribution, respectively.

Research	simulation	materials	velocity (m/s)	scale	validation type
Thornton et al. (1999)	aggl. particles (I)	E = 70GPa, ν = 0.35	0.1-0.9	⌀1.113mm	pattern
Kafui and Thornton (2000)	aggl. particles (I)	E = 70GPa, ν = 0.3	0.05-20	⌀0.461mm	pattern, mass dist.
Potapov and Campbell (2001)	spheres (I)	-	-	-	pattern, mass dist.
Mishra and Thornton (2001)	aggl. particles (I)	-	0.5-2	⌀0.44mm	-
Carmona et al. (2008)	spheres (I)	PMMA, PA, nylon	105-160	⌀16mm	pattern, mass dist.
Wittel et al. (2008)	spheres (I)	PMMA, PA, nylon	105-160	⌀16mm	pattern, mass dist.
Wittel (2010)	spheres (I)	concrete	120-200	⌀16mm	-
Wang and Tonon (2011)	cylinder dynamic (C)	granite	-	2.5×10cm	dyn. strength, size dist.
Bruchmüller et al. (2011)	sphere (DI)	plaster	-	⌀50-75mm	mass dist.
Paluszny et al. (2013)	sphere (I)	brittle rock	100-200	⌀100mm	pattern, mass dist.

Table 3: Example tabulated seeding parameters for impact velocity range of a 12.7 mm sphere.

$\Delta u_{i,c}$	x_c	m	S	ε
16.66	10.353	32.7691	(3,2,2)	0.0046
18.38	9.1668	15.6064	(4,2,2)	0.0921
23.68	5.5113	4	(4,4,6)	0.0858
24.66	4.8354	4	(4,5,8)	0.0353
25.32	4.3802	4	(5,5,10)	0.0386